Residual stresses induced by laser welding process in the case of a dual-phase steel DP600: Simulation and experimental approaches

A. Kouadri-Henni, C. Seang, B. Malard, V. Klosek

Residual stresses induced by laser welding process in the case of a dual-phase steel DP600: simulation and experimental approaches

[a]✉A. Kouadri-Henni[a], C. Seang[a], B. Malard[b], V. Klosek[c]

[a,]✉PSM Team (Correspondant author), Université Européenne de Bretagne, France, INSA, LGCGM, EA 3913, 20 Avenue des Buttes des Coësmes, F-35708 Rennes, FRANCE. afia.kouadri-henni@insa-rennes.fr, [b] Université de Toulouse, CIRIMAT, INP-ENSIACET, 4 allée Emile Monso - BP44362, 31030 TOULOUSE, [c]CEA de Saclay/DSM/IRAMIS/LLB

Abstract

This study aimed at characterizing the residual stresses distribution of a DP600 undergoing a laser beam welding. The residual stresses in the ferritic phase have been experimentally determined by the use of the neutron diffraction technique. The results confirmed a gradient of residual stresses among different zones both on the top and below surfaces but also through the thickness of the fusion zone. Low compressive stresses were observed in the BM (Base metal) close to the HAZ zone (Heat Affected Zone) whereas high tensile stresses were observed in the FZ (Fusion Zone). Two numerical modelling strategies were conducted: first with elastic plastic model (EP) and then with a visco-elastic plastic model (VEP) which takes into account the effect of phase transformation-induced volumetric strain. Both models allowed highlighting the residual stresses evolution through the different zones. Numerical results showed a difference in the residual stresses distribution depending on the model used. In the end, it appears that the high temperature, specific to the laser beam, is the main factor governing the residual stresses. When comparing simulation results with experimental data, the values converge well in some zones, in particular the FZ and the others less.

Keywords: Residual stresses, laser welding, DP600 steel, neutron diffraction technique, experimental and numerical approaches.

1. Introduction

Currently, industrial welding processes are rapidly evolving, this being driven by the need for process optimisation, cost effectiveness and ecological considerations. These are the reasons why laser welding has started to appear in production workshops, especially in the automotive, aeronautical and mechanical industries. This process is quick, precise and requires less energy in comparison with conventional welding processes. The DP600 steel is potentially useful because of its high mechanical characteristics which are 35% higher than usual steels [1, 2]. The use of this material allows a reduction in structural mass consequently to a decrease in thickness. Therefore, a decrease in fuel consumption could potentially be expected as well as a reduction in operational costs and emission of pollutants. Studies, related in this topic, have enabled a better understanding of the relationship between the welding process, the weld quality, the microstructure and the residual stresses evolution in the weld [3, 4]. In this welding process, the key parameter for microstructure optimisation and therefore mechanical properties appears to be the temperature and the heat transfer to the work pieces. These variations of mechanical properties have mainly been inputted to the initial manufacturing process of the base metal in the first place and then to the welding process. In all cases, numerous studies carried out in this field of research, have shown that there is a necessity to configure the welding process taking into account the fabrication history of the base metal, be it cast or rolled. In the case of laser welding, the key parameters are the ratios that control the temperature transfer; several studies have shown that this is a fundamental factor that governs the mechanical properties of the welded joints [5, 6]. For example, maximum strength of welds in DP600 is unaltered; however there is a diminution in the Yield Stress (YS) and in the elongation at failure. Most studies have shown the complexity of laser and associated heterogeneities. These mechanical heterogeneities have been explained by the initial fabrication method of the base metal (extrusion, casting,

rolling…) which determines the nature of the microstructure. This microstructure is with no doubt modified by the choice of the welding process [7, 8, 9]. From the mechanical point of view, and considering the initial nature of the base metal, results have shown an improvement or stabilisation of mechanical properties in the case of laser welding of DP600 steel [10, 11]. From the failure point of view, the failure of welded joints generally occurs in the base material, provided that the weld is of good quality. In the case of the laser welding process, failure generally occurs at the HAZ/BM interface [12]. Analysis of fracture features show that the failure areas are both ductile and brittle. These properties and differences in behaviour have been attributed to the influence of the microstructure on the mechanical behaviour and particularly regarding residual stresses [13, 14, 15]. Welding processes produce residual stresses which are linked to the rapid solidification but also to the mechanical environment such as the clamping of the work pieces. In the case of laser welding, tensile residual stresses are generally generated in the fusion zone [16].

The objectives of this study were then to study the evolution of the residual stresses of solid state phase transformation of dual phase steel DP600 in laser welding Nd:YAG by transparent mode. In this paper, experimental and numerical approaches are compared. Two approaches have been compared: experimental (neutron diffraction technique) and numerical. In the latest coupled thermo-metallo mechanical model was implemented in Abaqus software. The considered approaches were:

- For the thermal approach, conical heat source model with Gaussian distribution was used.

- For metallurgical approach, we used two physical models:

- Waeckel and Koistinen-Marburger model was used for modelling the austenitization and the cooling cycle during phase transformation of welding.

- The microstructure evolution (volume fraction of the ferrite, austenite and martensite) was used to calculate residual stresses in the welded joint and base metal.

• For mechanical approach, we used two models: an elastic plastic model (EP) and a visco-elastic plastic model (VEP) which takes into account the effect of phase transformation-induced volumetric strain.

The simulation revealed that the final phase that is under the influence of high speed welding gives higher volume fraction of martensitic phase in the FZ only on the top surface in addition with other volume fractions of austenite and ferrite that can be ignored. Because of the thin HAZ, a fine meshing of the HAZ is needed for accurate results. Finally the mean residual stresses in the different areas were identified in the ferrite which is the principal phase.

2. Experimental approach

2.1 Laser beam welding process

We used a laser beam, Nd:YAG, composed of the 4 kW generator with an arm robot type Fanuc R2000iB for welding operation. The diameter of the optical wire is 200 µm with a laser focus spot diameter of 560 µm and a focal length of 583.5 mm which corresponds to the focal point reference on the surface. Argon is used as a shielding gas with a flow rate of 20 CFH (Cubic Feet per Hour) on both surfaces of the blanks. To evaluate the properties of the welded joint such as the residual stresses, we welded by transparent mode two steel plates of both 1.25 mm thickness. The welding was conducted at a speed of 3.4 m/min and a power of 3.5 kW in full penetration mode with thickness of 2.5 mm for the overlapping area with a lap joint gap of 0.1 mm. The experiment conditions are presented in Figure 1.

2.2 Microstructure analysis

A metallographic cross section of a weld sample was prepared and examined for microstructural analysis under Leica optical microscope after etching it with a 4% Nital solution for 10 seconds, after what the samples were immediately washed with water followed by ethanol, and finally blown dry with hot air.

2.3 Residual stresses determination using neutron diffraction technique

The aim of the proposed experiments is to evaluate the residual stresses (σ_{11}, σ_{22} and σ_{33} of the stress tensor) by neutron diffraction in steel plates welded in lap joint configuration by laser welding. Experimentally, it is not possible to determine depth related variations using X-ray diffraction without removing material hence taking the risk to relax the residual stresses. Moreover, it was observed that the complex thermomechanical input induced complex stress gradients. So the high penetration capability of neutrons diffraction technique was used to determine stress profiles of the ferritic phase through the thickness and along the weld width. Figure 2 shows the obtained welded zones and the points where the measurements have been realized. We realized a scan through the welded zones: BM, HAZ and FZ on the mid plate in the longitudinal and transverse directions. The results were compared to our simulation model. Residual stresses were determined non-destructively by neutron diffraction measurements carried out on the dedicated 2 axis DIANE diffractometer at Laboratory Léon Brillouin (LLB) [17, 18]. A constant wavelength of 0.287 nm was used, allowing to record the {110} diffraction peak of the ferritic phase (Ferrite is a body centred cubic structure) at a diffraction angle of 2θ close to 90°, to obtained a parallelepipedic gauge volume. Strains were measured along the three principal directions (longitudinal, transverse and normal), defined by considering the geometry of the linear weld, at several locations with respect to the centre of the weld. Figure 3 gives the different studied zones on our sample (Fig. 3a) and the used

method (Fig. 3b) with the longitudinal, transversal. A gauge volume of 1x1x5 mm^3 was defined with the 5 mm aperture along the axis of the weld (to improve intensity), when possible (i.e. for transverse and longitudinal measurements only). The crystallographic texture of the base material was also determined by neutron diffraction technique on the dedicated 4-circles diffractometer 6T1 at LLB [18]. From the {110}, {200} and {211} pole figures, using a 5°x5° grid, the Orientation Distribution Function (ODF) was calculated using LaboTex software [19]. The texture exhibits slight {hkl}<110> reinforcements, typical of a cold rolled ferritic steel, but the calculated texture index is rather low (1.6). An elastic self-consistent calculation was performed considering the experimental texture to deduce the {110} dependent values for the Young modulus (E_{110}) and Poisson's ratio (ν_{110}): as a result, it appears that the elastic anisotropy should remain very low, with E_{110} ranging between 220 and 226 GPa, and ν_{110} ranging between 0.31 and 0.35, depending on the considered direction. In a first approach, biaxial residual stresses were calculated from the measured strains applying the Hooke's law (equation 1) in the isotropic elasticity approximation:

$$\sigma_i = \frac{E_{110}}{1+\nu_{110}}\left[\varepsilon_i + \frac{\nu_{110}}{1-2\nu_{100}}\sum_j \varepsilon_j\right] \quad (1)$$

where *i, j* = longitudinal, transverse and normal, and with the following values for Young modulus and Poisson's ratio: E_{110} = 220 GPa and ν_{110} = 0.33.

Since the characterized zones close to (Heat Affected Zone, HAZ) and within the weld (Fusion Zone, FZ) may have their microstructures more or less strongly affected by the welding process, chemical composition is likely to be heterogeneous depending on the distance from the centre of the weld. One would thus commit an error if considering the base material as the reference material for unstrained lattice spacing. So, due to the low thickness of the studied plates, a zero normal stress state was assumed (i.e. a plane stress state), and

theoretical reference lattice spacing and diffraction angles $2\theta_0$ could thus be calculated for each measurement point, applying the following formula, [20]:

$$2\theta_0 = 2 \cdot \sin^{-1}\left(\frac{(1+\nu) \cdot \sin\theta_{normal} \cdot \sin\theta_{axial} \cdot \sin\theta_{transverse}}{(1-\nu) \cdot \sin\theta_{axial} \cdot \sin\theta_{transverse} + \nu \cdot \sin\theta_{normal} \cdot (\sin\theta_{axial} + \sin\theta_{transverse})} \right) \quad (2)$$

Considering the difficulty to obtain a reliable unstressed reference sample, the reference (unstressed) $d_{0,\{110\}}$ lattice spacing required for strain calculations was determined assuming a zero normal stress at 5 mm in the base metal from the centre of the weld.

3. Numerical approach: thermo-metallo-mechanical model

The thermo-metallo-mechanical model is composed of three separate models, the thermal model, the metallurgical model and the mechanical model.

3.1 Simulation parameters

The meshing dimension along the welding direction DX is fixed to 0.3125 mm. In the transverse direction DY, the mesh size is 0.2 mm in FZ and 0.175 mm in HAZ and progressive mesh in the BM. The mesh dimension in the direction DZ is 0.3125 mm. The quadratic mode is used for the thermal analysis and the linear mode for the metallurgical analysis of the thermo-metallurgical simulation of dual phase steel DP600 (2.5 mm x 50 mm x 110 mm) within transparent mode including 0.1 mm gap as presented in the figures 4 and 5 for the clamping conditions (Fig.5a). From a thermal model point of view, the boundary conditions are the convection and radiation with the surrounding environment applied in the cooling step as presented in figures 5b and 5c. The values of mesh dimension are summarized in Table 1. The thermo-metallurgical simulation is done in two steps. The welding step takes

0.8818 seconds and the cooling step 120 seconds. The values of materials properties used for thermal and mechanical FE analyses are summarized in the tables 2 and 3.

3.2 Thermal model

The heat transfer from the volumetric heat source to the metal during the welding phase is expressed in equation 3:

$$\rho\frac{dH}{dt} - \mathrm{div}(\lambda \mathrm{grad}T) - Q = 0 \quad (3)$$

With:

H enthalpy ($J.kg^{-1}.°C^{-1}$) which depends on C_p specific heat capacity ($J.\ kg^{-1}.{}^{o}C^{-1}$),

T temperature (°C),

λ thermal conductivity ($W.m^{-1}.°C^{-1}$),

Q heat source density ($W.m^{-3}$),

ρ density ($Kg.m^{-3}$).

The heat losses during the cooling process (convection and radiation) have been expressed by two mathematical formulations 4 and 5:

- The convection limit conditions in the surrounding environment are given by:

$$\lambda(T)\mathrm{grad}T(x_i,t)_{surface} + h(T(x_i,t) - T_0) = 0 \quad (4)$$

- The radiation limit conditions on the surface of the weld pool are given by:

$$\lambda(T)\mathrm{grad}T(x_i,t)_{surface} + \varepsilon\sigma(T(x_i,t)^4 - T_\infty{}^4) = 0 \quad (5)$$

With:

σ : Stefan Boltzmann constant ($W.m^{-2.\,\circ}C^{-4}$)

ε : Emissivity of the radiating surface

h : heat transfer coefficient ($W.m^{-2}.\,°C^{-1}$)

An initial condition is defined by the temperature (T_0°C) of metal which is equal to the ambient temperature 20°C. The conical heat source with a Gaussian distribution has been chosen (Figure 6). The members of all used equations, the parameters used in the conical heat source and all symbols used are detailed in Table 4. The conical heat source with a Gaussian distribution [21] used in modelling is represented by the following equations (6 and 7):

$$Q(r,z) = \frac{9\eta Pe^3}{\pi(e^3-1)} \cdot \frac{e^{-[\frac{3r^2}{r_c^2}]}}{(z_e - z_e)(r_e^2 + r_e r_i + r_i^2)} \quad (6)$$

With

$$r_c = r_i + \frac{(r_e - r_i)(z - z_i)}{z_e - z_i} \quad (7)$$

The thermal model is constituted of the heat transfer equation and the heat source model.

3.4 Metallurgical model

3.4.1 Metallurgical model choice

The chosen model for the metallurgical items is the Waeckel's model [22, 23]. It allows describing the anisothermal-metallurgical transformation provided by a differential equation. This model derived from Leblond's model [13], based on the Continuous Cooling Transformation (CCT) diagram data, which is particularly suitable to describe the industrial

applications such as welding. It is able to simulate all thermo-metallurgical histories and has been inserted in the thermo-mechanic finite element code, Code Aster. This model is easier than Leblond's model for identifying the parameters. During heating, the only transformation able to occur is the transformation into austenite which does not strongly depend on the heating rate. Then the function used to describe this kind of transformation is the same as those proposed by Leblond (equation 8) and for which:

$$\dot{Z}_\gamma = \frac{Z_{eq} - z_\gamma}{\tau(T)} \tag{8}$$

Where:

z_γ denotes the austenite proportion,

Z_{eq} is the change in the rate of austenite transformed during quasi-static evolution,

τ represents the growth parameter (second).

Z_{eq} and τ are two functions depending on temperatures (equations 9 and 10).

With

$$Z_{eq}(T) = \begin{cases} 0 & \text{if } T \leq Ac1 \\ \dfrac{T - Ac1}{Ac3 - Ac1} & \text{if } Ac1 \leq T \leq Ac3 \\ 1 & \text{if } T \geq Ac3 \end{cases} \tag{9}$$

And

$$\tau(T) = \begin{cases} \tau_1 & \text{if } T \leq Ac1 \\ \tau_1 + \dfrac{T - Ac1}{Ac3 - Ac1}(\tau_3 - \tau_1) & \text{if } Ac1 \leq T \leq Ac3 \\ \tau_3 & \text{if } T \geq Ac3 \end{cases} \tag{10}$$

The values of $\tau_1 and\ \tau_3$, which were determined experimentally, correspond to the time for quasi static temperature of the start (Ac_1) and the end (Ac_3) of austenite transformation. The volume fraction functions, equation 8, are resolved using the Euler explicit methods as the expressions (11 and 12):

$$Z_{n+1} = Z_n + \dot{Z}_n.\Delta t \tag{11}$$

$$\Delta t = t_{n+1} - t_n \tag{12}$$

Where Z_{n+1} is the new volume fraction at the increment time n+1, Z_n is the volume fraction at the increment time n and Δt is the increment time. During rapid cooling, the austenite with a face centred cubic structure changes to martensitic phase with a body centred tetragonal structure. This phase transformation is described by the Koistinen and Marburger model (equation 13).

$$z_m = z_0[1 - \exp[-\beta\langle M_s - T\rangle]] \tag{13}$$

Where $\langle x\rangle = 0\ \forall x < 0\ et\ \langle x\rangle = x\ \forall x \geq 0$,

z_m is the proportion of martensite formed,

z_0 is the initial proportion of austenite,

Ms is the martensitic start temperature,

β is a material parameter and

T is the temperature in degree Celsius.

3.4.2 Boundary conditions and parameters

The thermo-metallurgical simulation was done in two steps. Each step corresponds to a specific time of welding and cooling as presented below:

- The welding step : 0.8818 s
- The cooling step: 120 s
- Mean time for $\tau_{8/5}$: 0.7 s
- β of the Koistinen-Marburger model: 0.2

These parameters used in this simulation were obtained from the results of thermal simulation and from the literature [10, 11, 16]. The values of these parameters are presented in table 5. The boundary conditions that include the convection and radiations (surrounding environment) are described by the equations (4, 5) and have been applied in the cooling step.

3.5 Mechanical model: residual stresses

The separation between the volume change and the thermal deformation rates by changing the coefficient of thermal expansion allows having the flexibility to describe the behaviour of the material. The phase transformation plays an important role in modelling residual stresses [4].

3.5.1 Simulation and parameters

The simulation is done in two states, the thermal and mechanical states, where three steps are considered, the welding step for 0.8823 seconds, the cooling step for 120 seconds and the relaxing step for 120 seconds with a laser power of 3.5 kW and a laser speed of 3.4 m/min. A quadratic interpolation function gives more accurate results close to the weld seam and is used in this simulation to solve the thermal analysis of welding. Linear interpolation was used to solve the mechanical analysis. Two mechanical models are used here, the elastoplastic model

(EP model) and the elastoplastic with transformation induced volumetric strain model (VEP model). The simulation of these two models was done at the same condition and meshing parameters in order to evaluate their different outputs such as residual stresses (see table 6).

3.5.2 Resolution

The resolution of the mechanical equation is based on the equation (14) of static equilibrium:

$$\mathrm{div}(\sigma) - \mathrm{F} = 0 \qquad (14)$$

Where σ is the stress tensor and F is the volumic force. The relationship of deformation is described in the following case (equation 15):

$$\varepsilon = \varepsilon^{e} + \varepsilon^{th} + \varepsilon^{p} + \varepsilon^{VEP} \qquad (15)$$

where ε^{e} is the elastic strain, ε^{th} is the thermal strain, ε^{p} is the plastic strain and ε^{VEP} is the transformation induced volumetric strain. The separation between the transformation induced volumetric strain and the thermal strain by changing the thermal expansion coefficient allows having more flexibilities to describe the behaviour of the material [9]. The phase transformation plays an important role in modelling the residual stresses. To count for these changes in volume, the thermal deformation is replaced by a thermo-metallurgical strain or transformation induced volumetric strain [23, 24], described in the equation (16):

$$\varepsilon^{thm} = (1 - Z).\left(\alpha_{\gamma}(T - T_{\gamma ref}) - \Delta\varepsilon_{\alpha\gamma}^{20°C}\right) + Z.\left(\alpha_{\alpha}(T - T_{\alpha ref})\right) \qquad (16)$$

Where Z is the proportion of α ferritic phase, $\varepsilon_{\alpha}^{th}$, $\varepsilon_{\gamma}^{th}$ are respectively the thermal expansion of the ferritic phase α and austenitic phase γ. $\Delta\varepsilon_{\alpha\gamma}^{20°C}$ is the different thermal strain between the two phases. The volume change of DP600 steel from austenite to ferrite is

assumed to be 1.4% and from austenite to martensite to be 1% which is in accordance with values reported in the researches [23, 24]. The boundary condition plays an important role in the formation of residual stresses and deformation of the welded joint. The nature of contact surface between the clamping system and the sheet metal is also influenced by the cooling rate of the welding process (Figure 7). A case performed by Shrenk [25] showed that cooling factor can be increased up to a factor of two following the nature of contact. The influence of the distance and the force of the clamping as well as the release time after welding have been studied by many authors [26, 27]. There are some compromise and contradiction of the clamping position on the distortion prediction. The Boundary Conditions (BCs), as illustrated in Figure 7a, used in this model are:

- Positions 1, 2, 4 and 5: Displacement Z =0 *(Z-SYMM mode)*. These BCs *(BCs at positions 1, 2, 4 and 5)* will relax at third step.
- Position 3: Lock the start of weld seam *(Clamp-mode)* and displacement Z = 0 *(Z-SYMM-mode)* at the end of weld beam. These BCs are locked for all steps. The model is separated into three zones, the FZ, the HAZ and the BM. The first order element with 8-nodes brick technique is used for the HAZ and the FZ in purpose to assure a constant and small element size inside these two zones. On the other hand the sweep technique with advancing front algorithm is used to reduce the number of elements inside the BM as shown in Figure 7b. Mesh dimension of the FZ and the HAZ have been already presented in the table 6. To be in accordance with the experiment, we made an average of the numerical results taking into account the same gauge volume in the mid plates.

3.5.3 Calibration and verification of the simulation model

3.5.1 Dimension of weld bead

Figure 8 shows the half model of thermal simulation and of experimental sample. The figure 8a shows the temperature simulation during the welding. The macroscopic image (Fig.8b) of the weld cross section allows identifying the dimension of FZ and the HAZ zones which were then compared with the simulation (Fig.8c). Comparing experimental and simulation prediction, we can see that a good correlation was achieved.

3.5.2 Temperature field

The temperature evolution on the top surface in the vicinity of the lap joint was measured by three K-type (Chromel-Alumel) thermocouples with wire diameter of 300 micrometers. Those thermocouples are fixed to the top sheet metal by resistance spot welding technique as indicated in Figure 9a. Temperature acquisition during welding and cooling process was made by NI-DAQ, NI-9214 of National Instruments, which is capable of treating 16 differential inputs from thermocouple. The accuracy of temperature measurement for NI-9214 is $0.02^{o}C$ and the accuracy of K-type thermocouple is $1.1^{0}C$ in the range of $-180^{0}C$ to $+ 1300^{o}C$. The temperatures evolution curve, described in Figure 9b, shows the evolution of temperature during welding and cooling cycle at three points 1 (TC1), 2 (TC2) and 3 (TC3) got from experimental and numerical analysis. The evolution of temperature from the simulation is similar to the experiment (less than 10%).

4. Experimental results

4.1. Microstructure evolution

Optical metallography was carried out to observe the variation of microstructure content in the different zones (Figure 10). From the microstructure point of view, this process leads to three distinct zones: the base metal (BM), the heat affected zone (HAZ), the fusion zone (FZ). Figure 10 shows the microstructure evolution on the top surface in the different zones. The

BM is mainly constituted of ferritic phase (grains with white colour, Fig.10a). The HAZ near the BM stays unchanged (Fig. 10b, b-HAZ) compared to the BM. Very near to the FZ in the c-HAZ zone (Fig. 10c), the volume fraction of ferritic phase decreases from the HAZ to almost zero in the FZ (fig. 10d). The latter zone is dominated by the volume fraction of martensitic phase. These observations confirm the presence of microstructure gradient on the top surface. These results are in agreement with both the metal nature and the used process. In fact, the welding speed influences the cooling time, $t_{8/5}$, which is an important factor of the martensitic, ferritic and austenitic phases formation. Based on the CCT diagram, the formation of pearlite occurs at a very slow cooling time compared to the formation of bainite and ferrite. Thus it is impossible to have the transformation of bainite and pearlite from austenite in the DP600 steel with laser welding at high speed. The coarsening martensitic phase observed in the FZ is higher compared to the HAZ because of the degree of coarsening that increases with a higher degree of austenitization temperature during the cooling phase after laser welding. Figure 11 shows the microstructure evolution through the thickness of the fusion zone. Figures 11a and 11b present the global zone of the full penetration of our welding. From the welded zone point of view, the FZ has a grain refinement which is roughly smaller than the BM and the HAZ regions (Fig. 11c). The FZ is constituted of a number of different phases. The principal phase in this zone is the ferritic phase. The martensitic phase is still present and represents less than 13% of the BM. Finally the observations have shown that the martensitic phase is localised at the grain boundaries (Fig. 11d). This fraction corresponds to that of the initial BM.

4.2 Residual stresses evolution in the ferritic phase:

Figures 12 and 13 present the longitudinal and transverse residual stresses in the ferrite in the mid steel plate. The numerical and experiment results are compared. To be in accordance with the experiment, we made an average of the numerical results taking into account the same gauge volume in the mid plates.

4.2.1 Experiment results

An increase in the tensile transverse (σ_{11}) residual stresses (figure 12) is observed in the FZ (about 289 MPa). The magnitudes of maximum residual stresses are located in the FZ and a decreasing in the HAZ. This is the well-known evolutions that were generally described in laser residual stresses [21]. These observations are due to the higher and lower temperatures generated respectively in the FZ and in the HAZ, leading to a temperature gradient occurring in a narrower zone hence generating higher residual stresses. Moreover, asymmetric stresses profiles are observed in the transverse stresses in the left and right HAZ zone. These are due to the asymmetry of the geometry of the weld (see Figures 2 and 3). The longitudinal residual stresses,σ_{22}, (Figure 13) already dominate by values higher than those of the transverse residual stresses (about 480 MPa). This is consistent with previous studies [21, 22, 23, 24].

5. Numerical results: Residual stresses evolution in the ferritic phase

The magnitude of residual stresses after welding is important in the prediction of resistance to fracture [28]. To study the different residual stresses got from the elastoplastic model (EP model) and the elastoplastic with volume change model (VEP model), one has to care about: the Von Mises stresses (VM), the transversal stresses σ_{11}, the longitudinal stresses σ_{22} along the transverse and longitudinal lines of the welding at the end of cooling cycle.

5.1 Residual stresses in the ferrite along the transverse line of welding direction

Figure 12 presents the variation of residual stresses. The influence of transformation induced volumetric strain is observed based on the comparison of the residual stresses (VM, σ_{11}, σ_{22}) analysis of the EP model and those of the VEP model. The magnitudes of maximum residual stresses of these two models are located in the FZ and a decreasing in the HAZ which are almost dependent on the ambient temperature yield strength: about 490 MPa for the VM model and 370 MPa, 311 MPa respectively for the EP and VEP models (Figures 12 and 13). The experiment results give a maximal value of 290 MPa. The general aspects of residual stresses of these models and of the experiments are almost similar but a few different aspects of residual stresses are found. The residual stresses distribution along the transverse direction of VM model is wider and higher than that of the EP and VEP models (Figure 12). The experiment results of transverse residual stresses seem closer to the EP/VEP models than that of VM model. The figure 14 shows the average of the residual stresses for every model in the FZ and the figure 15 for the HAZ.

5.2 Residual stresses in the ferrite along the longitudinal line of the weld

The residual stresses along the longitudinal line, σ_{22}, (along the weld center line) are shown in Figures 13. The distribution of residual stresses of EP model and VEP model are almost similar. Along the longitudinal line inside the FZ of the weld seam centre, the EP model gives a higher level of longitudinal stresses (σ_{22}) than that of the VEP model. The VM model gives higher values. From the result point of view, in the longitudinal direction of welding, the residual stresses (VM, σ_{11}) present higher and constant values in the fusion zone of about 500 MPa for the VM model and about 300 MPa and 350 MPa respectively for EP and VEP model. The experiment results give a maximal value about 470 MPa. In this case, it seems that the

VM model is more appropriated. The principal difference between the experiment and numerical approach found is the start and end point of the weld bead.

In conclusion, these results are coherent and in agreement with those found in the literature [29, 30]. With laser beam, the temperature is uniform along the weld length but the temperatures in the transverse direction are non-uniform. The principal result is that the numerical approach takes into account the non-asymmetric configuration and gives an appropriated range of residual stresses.

6. Discussion

In the present study, a DP600 steel material used in the automotive industry has been analysed in order to evaluate the residual stresses due to welding done by high power laser. Laser beam welding process includes high heat radiation and convection losses. The laser beam gets embedded inside the molten metal within the dead end capillary key hole and loses energy which is mostly transmitted by heat conduction and also by absorption. These phenomena lead to several consequences such as metallurgical and mechanical modifications [28, 29]. To understand the laser welding effect on residual stresses, we worked with two approaches: numerical and experimental. We used ABAQUS software for the simulation model. The coupled thermal model to mechanical model, taking into account the metallurgy effect, was used to compare the residual stresses evolution with experiments. Experimentally, residual stresses induced by laser welding were determined by neutron diffraction technique. Residual stresses distribution on the mid plate through the thickness, at the centre of the small Fusion Zone (FZ), in the heat affected zone (HAZ) and in the base metal (BM) were calculated.

6.1 Experimental results

Experimentally, we realized the measurements in the mid plate of the weld bead in transversal and longitudinal direction. Experiment results showed the average calculated values of residual stresses in the various zones for the laser welding process and in different stresses directions: longitudinal, transversal. The BM has low values of tensile residual stresses in the order of 0 MPa to 20 MPa. These values, identical for both sides, showed that the BM is homogeneous. For the HAZ zone, an asymmetric distribution of residual stresses between the two sides is observed. This observation is the same for the two approaches: experiment and numerical. For the left side of the welding, the transverse residual stresses in the HAZ decreases but stays around 200 – 250 MPa. On the right side of the weld, the same evolution is observed with a higher decreasing of tensile residual stresses in the HAZ. They are relatively low and near (70 MPa) for the experiment and EP/VEP models while they stay high for the VM model (about 250 MPa). The comparison between the three zones (BM, ZAT and FZ) showed that lower stresses are obtained in the BM, tensile stresses in the FZ and in the HAZ. These stresses are principally generated by the high thermal gradient that is a maximum and constant in the longitudinal direction and gradually decreasing in the transversal direction.

The welding process influenced the residual stresses distribution. The residual stresses variation appears to be in correlation with the nature of the heat flux and the rapid cooling kinetics which are associated with the laser process. These evolutions are in agreement with the literature [30, 31, 32, 33]. The temperature near the FZ and HAZ rapidly changes as the distance increases from the heat source. The variation of residual stresses follows the thermal cycle of laser process. The principal difference between the experiment and numerical approach found is the start and end point of the weld bead following the used model. In the longitudinal direction residual stresses are tensile and constant. The distribution is almost the

same for all approaches. Regarding the non-symmetrical values in the HAZ, this phenomena can be explained not only by the thermal gradient due to laser process but by the mechanical configuration of welding which is non-symmetrical (configuration with wink) and so due to the asymmetric clamping [31, 32, 33].

6.2 Numerical results

Numerically, from the residual stresses point of view, we used two models: the elastoplastic model (EP model) and visco-elastoplastic (VEP model). From the thermal model point of view, we first considered a constant heat flux and in a second step considered a Gaussian flux from a laser beam source taking into account the transient temperature distribution [15, 16, 21]. Several authors [30, 31] used different simulation tools to model non-linear transient three dimensional heat transfer model for the CO_2 or Nd:YAG laser welding simulation for different alloys. From an only mechanical point of view, the phase transformation has been taken into account through the thermal strain (ε^{th}), which gives the influence of transformation induced volumetric strain. The temperature dependent thermal-mechanical properties are used in the simulation. In the first place, we have realized the comparison of the numerical residual stresses (VM, σ_{11}, σ_{22}) between these two models: VE and VEP. Then, we discussed the experimental and numerical results.

Numerically, from a stress point of view, the comparison of the residual stresses (VM, σ_{11}, σ_{22}) analysis of the EP model and those of the VEP model has been realized. The general aspects of residual stresses of these models are almost similar and only few differences in residual stresses were found. The longitudinal residual stresses distribution of VM model is wider than that of the EP/VEP model. The results confirm that the laser welding lead to a

constant temperature in the longitudinal direction. In this case, the Von Mises modem seems to be in line with the experiment approach. In the FZ, the longitudinal residual stresses (σ_{22}) present higher values in the order of 500, 480, 370 and 300 MPa respectively for VM, experiment results, EP and VEP models. The experiment results are near of those of VM model. The principal difference between the experiment and numerical approach found is the start and end point of the weld bead following the used model. In the transversal welding direction, both models give again the same results for the EP/VEP models and near of σ_{11} stresses. The magnitudes of maximum and minimal residual stresses of these two models are located in the FZ and HAZ respectively. These results are coherent and in agreement with those found in the literature [4, 7, 17, 19, 32, 33]. In fact, with laser beam, the temperature is uniform along the weld length but the temperatures in the transverse direction are non-uniform: the temperature decreases from the FZ (maximal temperature) to the BM (ambient temperature). Numerical results such as the experiment revealed a non-symmetrical pattern of stress values in the HAZ: on the left-hand side the values are slightly lower than on the highly-rated right-hand side. The numerical model takes into account the conditions imposed for the clamping which is necessary in the case of this configuration of welding [32, 33].

6.3 Comparison between numerical and experimental results

Residual stresses distribution between the different approaches and models showed a same distribution with some differences. These differences can be explained by various effects which we cannot deconvolve with the experiment and the some effects not taken by numerical approach. For example, the metallurgical transformation gradient [10, 11, 13] has to be controlled. The quantity of martensite on the above steel plate is higher than on the below one. This difference is due to the higher solidification speed on the above steel plate. From

our results, it seems that a higher quantity of martensitic phase could relax the residual stresses [2, 3, 4, 5, 11, 23, 24]. It is a way we would like to investigate in a more precise manner in a next work which could lead to a better understanding of the influence of the martensitic and austenite phase on the residual stresses.

Experimental and numerical results showed the same trends considering the residual stresses in the ferrite and the studied zones. For each butt welding parameter studied, similar curves were obtained. The study in the transversal direction gives the same distribution: BM and HAZ with low values. In comparison, experimental results give the same results in the FZ but show a difference in other zones (BM and HAZ), where the residual stresses are lower. We think that the observed differences are due to the transformation of the ferritic phase to austenitic and martensitic phases [10, 11, 13, 23, 24]. In fact, high tensile residual stresses were induced by the laser welding operation. This strong stress gradient is not fully predictable by the simulation which can only determine mean stress values. The difference can also be explained by the incompatible strain leading thermal stresses. These incompatible strains, due to dimensional changes associated with solidification of the weld metal, metallurgical transformations and plastic deformation, are the main factor that can explain differences between simulation and experiment methods, highlighted in some given locations. The number of coupled effects in welding during temperature distribution eventually led the structural changes, exhibited by generation of residual stresses [2, 3, 4, 5].

7. Conclusion, prospects and future developments

This study focused on the residual stresses generated by laser beam on a DP600 steel. During laser welding, the parts are locally heated by an intense laser beam followed by melting and solidification. In our work, the residual stresses of a 3 mm thick plate are simulated and then validated with experiments using neutron diffraction technique. The major contribution of this study is the comparison between two approaches: numerical and experiment. We studied the characterization of the residual stresses influenced by the LBW process, the microstructure and mechanical evolution due to the high thermal gradient generated by laser welding process. A first development arising from our work would be to consider the residual stresses taking into account principally the heat input generated by laser beam. Our results confirm that the temperature seems to be the main factor that explains the residual stresses in the ferritic phase of the welded specimens presented. Nevertheless, the model does not reproduce real welding procedure, namely in terms of high gradient thermal and several metallurgical modifications due to the nature of the welding process. The microstructure dependent on both mechanical and thermal properties has to be taken into account to get better correlation between numerical and experimental results. A more complex model in progress is to be implemented in order to consider others factors. Then, for the further residual stresses analysis, the influence of the anisotropy and phase transformation will be studied and stress calculations will be done taking into account others parameters. Moreover, one needs to consider the influence of the parameters of the process. For example, Georgeta et al., (2012) [34] found that residual stresses of laser welding increase with higher laser beam power and reduces with higher welding speed as with higher spot diameter.

A second development arising from our work would be to consider the residual stresses taking into account other parameters: phase transformation during the welding i.e. the presence of martensitic and austenitic phases. As well as the high quantity of martensitic phase after the welding, the laser is expected to influence in a deeper way the global mechanical properties and in particular the residual stresses. Moreover, it would be worth studying weld behaviour of steel. A direct development of our work would be to develop modelling aspects, especially regarding LBW, taking into account residual stresses and crystallographic texture evolution. It must be added however that the clamping tooling might be the source of additional structure modifications (relaxation or shrinkage) during the welding process, hence the creation of a new residual stresses field. This effect could enhance the correlation between the simulation and experimental results.

REFERENCES

[1] D. Radaj et al. Welding residual stress and distorsion: calculation and measurement, DVS 2003.

[2] A. Murugaiyan, A. Saha Podder, A. Pandit, S. Chandra, D. Bhattacharjee, and R.K. Ray. Phase transformation in two c-mn-si-cr dual phase steels. ISIJ International, 2006; 46:1489–1494.

[3] E. Biro, J. McDermid, J. Embury, and Y. Zhou. Softening kinetics in the subcritical heat-affected zone of dual-phase steel welds. Metal. and Mater. Trans. A, 2010; 41:2348–2356.

[4] D. Deng. Fem prediction of welding residual stress and distorsion in carbon steel considering phase transformation effects. Mater. & Des, 2009; 30(2):359 – 366.

[5] N. Farabi, D.L. Chen, J. Li, Y. Zhou, and S.J. Dong. Microstructure and mechanical properties of laser welded DP600 steel joints. Mater. Sc. and Eng. A, 2010; 527(4-5):1215 – 1222.

[6] Q. Sun, H-S Di, J-Ch Li, B-Q Wu, R.D.K. Misra. A comparative study of the microstructure and properties of 800 MPa microalloyed C-Mn steel welded joints by laser and gas metal arc. Mater. Sc. and Eng. A, 2016; 669: 150-158.

[7] D. Gery, H. Long and P. Maropoulos. Effects of welding speed, energy input and heat source distribution on temperature variations in butt joint welding. J. of Mater. Proc. Tech., 2005; 167(2-3):393–401.

[8] S. Kumar, R. Awasthi, C.S. Viswanadham, K. Bhanumurthy, G.K. Dey. Thermo-metallurgical and thermo-mechanical computations for laser welded joint in 9Cr–1Mo(V, Nb) ferritic/martensitic steel. Mater. & Des., 2014;59: 211-220.

[9] C. Grignon, E. Petitpas, R. Perinet and Jean Condoure. Thermometallurgical modeling applied to laser welding of steels. Inter. J. of Therm. Sc., 2001; 40(7):669 – 680.

[10] J.Trzaska, A.Jagietto, and L.A. Dobrzanski. The calculation of CCT diagrams for engineering steels. World Acad. of Mater. Sc. and Manu. Eng., 2009; 39:13–20, 2009.

[11] D.P. Koistinen and R.E. Marburger. A general equation prescribing the extent of the austenite-martensite transformation in pure iron-carbon alloys and plain carbon steels. Act. Metal., 1959; 7(1):59 – 60.

[12] V.H Baltazar Hernandez, Sushanta Kumar Panda, Yasuaki Okita, and Norman Y Zhou. A study on heat affected zone softening in resistance spot welded dual phase steel by nanoindentation. J. of mater. Sc., 2010; 45:1638–1647.

[13] J.B. Leblond and J. Devaux. A new kinetic model for anisothermal metallurgical transformations in steels including effect of austenite grain size. Act. Metal., 1984; 32(1):137 – 146.

[14] G. Mi, L. Xiong, C. Wang, X. Hu, Y. Wei. A thermal-metallurgical-mechanical model for laser welding Q235 steel. J. of Mater. Proc. Tech., 2016; 238: 39-48.

[15] P. Martinson, S. Daneshpour, M. Koçak, S. Riekehr, and P. Staron. Residual stress analysis of laser spot welding of steel sheets. Mater. & Des., 2009; 30(9):3351 – 3359.

[16] Y. Javadi, M. Akhlaghi, M.A Najafabadi. Using finite element and ultrasonic method to evaluate welding longitudinal residual stress through the thickness in austenitic stainless steel plates. Mater. & Des., 2013;45:628-642.

[17] D.W. Brown, J.D. Bernardin, J.S. Carpenter, B. Clausen, D. Spernjak, J.M. Thompson. Neutron diffraction measurements of residual stress in additively manufactured stainless steel. Mater. Sc. and Eng, 2016; 678A: 291-298.

[18] J.P. Oliveira, F.M. Braz Fernandes, R.M. Miranda, N. Schell, J.L. Ocaña**.** Residual stress analysis in laser welded NiTi sheets using synchrotron X-ray diffraction**.** Mater. & Des., 2016; 100: 180-187

[19] K. Pawlik, P. Ozga: “LaboTex: The Texture Analysis Software”, Göttinger Arbeiten zur Geologie und Paläontologie, SB4, 1999.

[20] P. Staron, M. Koçak, S. Williams, A. Wescott, Physica B 350 e491, (2004).

[21] M. Z. Ul Abdein, D. Nelias, JF Jullien and D. Deloison. Prediction of laser beam welding-induced distortions and residual stresses by numerical simulation for aeronautic application. J. of Mater. Process. Techn., 2009; 209(6):2907 – 2917.

[22] A. Laamouri, H. Sidhom, C. Braham. Evaluation of residual stress relaxation and its effect on fatigue strength of AISI 316L stainless steel ground surfaces: Experimental and numerical approaches. Intern. J. of Fatigue, 2013; 48:109-12.

[23] P. Dupas F. Waeckel and A. Andrieux. Thermo-metallurgical model for steel cooling behaviour: Proposition, validation and comparison with the sysweld's model. J. of physique IV(6), EDP Sciences,1996.

[24] Mingsheng XIA and Elliot BIRO. Effects of heat input and martensite on haz softening in laser welding of dual phase steels. ISIJ International, 2008; 48(6):809–814.

[25] C. Heinze, C. Schwenk, M. Rethmeier, Numerical calculation of residual stress development of multi-pass gas metal arc welding, J. of Constructional Steel Research, 2012; 12-19.

[26] G. Chen, L. Mei L, M. Zhang, Y. Zhang, Z. Wang. Research on key influence factors of laser overlap welding of automobile body galvanized steel. Opt. Laser Tech.2012; 45: 4146-4155.

[27] QS. Liu, SM. Mahdavian, D. Aswin, S. Ding. Experimental study of temperature and clamping force during Nd:YAG laser butt welding. Opt. Laser Tech., 2009; 41: 794-799.

[28] Xiangzhong Jin, Lijun Li, An experimental study on the keyhole shapes in laser deep penetration welding, Opt. and Lasers in Eng., 2004; 44: 779–790.

[29] Q. Wu, J. Gong, G. Chen, L. Xu. Research on laser welding of vehicle body. Opt. Laser Techn., 2008; 40: 420-6.

[30] Shusen Zhao, Gang Yu, Xiuli He, Yongjie Zhang, Weijian Ning. Numerical simulation and experimental investigation of laser overlap welding of Ti6Al4V and 42CrMo. J. of Mater. Process. Techn., 2011; 211:530–537.

[31] A.P. Mackwooda, R.C. Craferb, Thermal modelling of laser welding and related processes: a literature review Opt. & Laser Techn., 2005; 37:99 – 115.

[32] J.M. Costa, J.T.B. Pires, F. Antunes , J.P. Nobre , L.P. Borrego. Residual stresses analysis of ND-YAG laser welded joints. Eng. Failure Anal., 2010; 17(1); 28-37.

[33] J. Sun, X. Liu, Y. Tong, D. Deng. A comparative study on welding temperature fields, residual stress distributions and deformations induced by laser beam welding and CO_2 gas arc welding. Mater. & Des., 2014; 63:519-53.

[34] A. Georgeta, S. Gheorghe S, I. Danut, Input Parameters Influence on the Residual Stress and Distortions at Laser Welding Using Finite Element Analysis, UPB Scientific Bulletin, Series D, 2012; 74(2): 15.

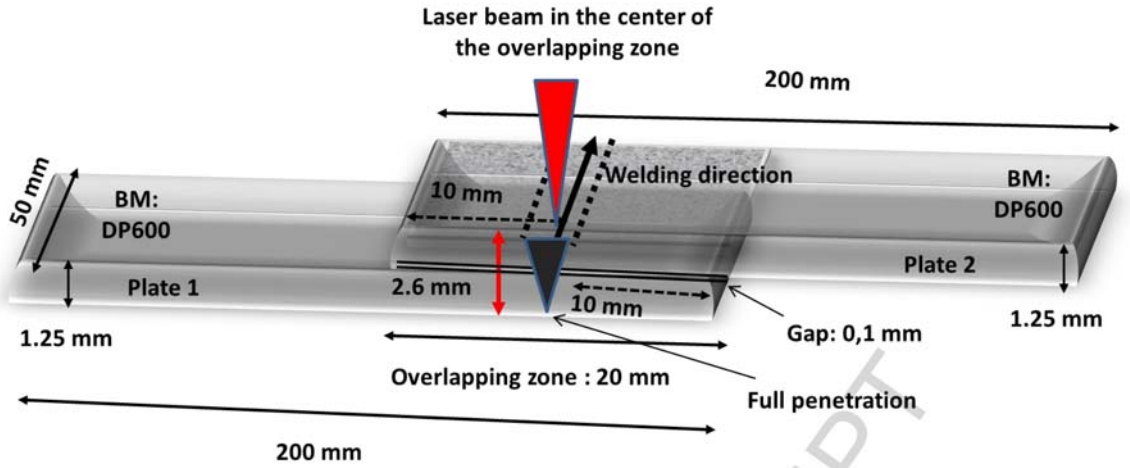

Fig.1: Conditions of laser welding, geometry and dimensions of sample

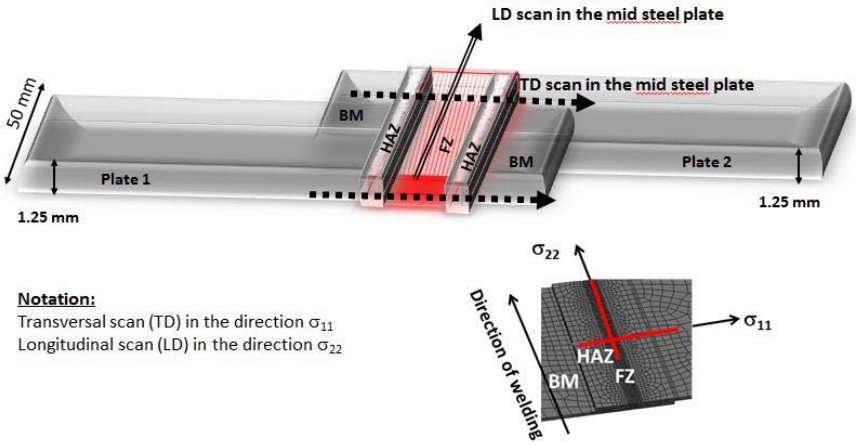

Fig.2: Measurement points and direction scans in the different zones: BM, HAZ and FZ

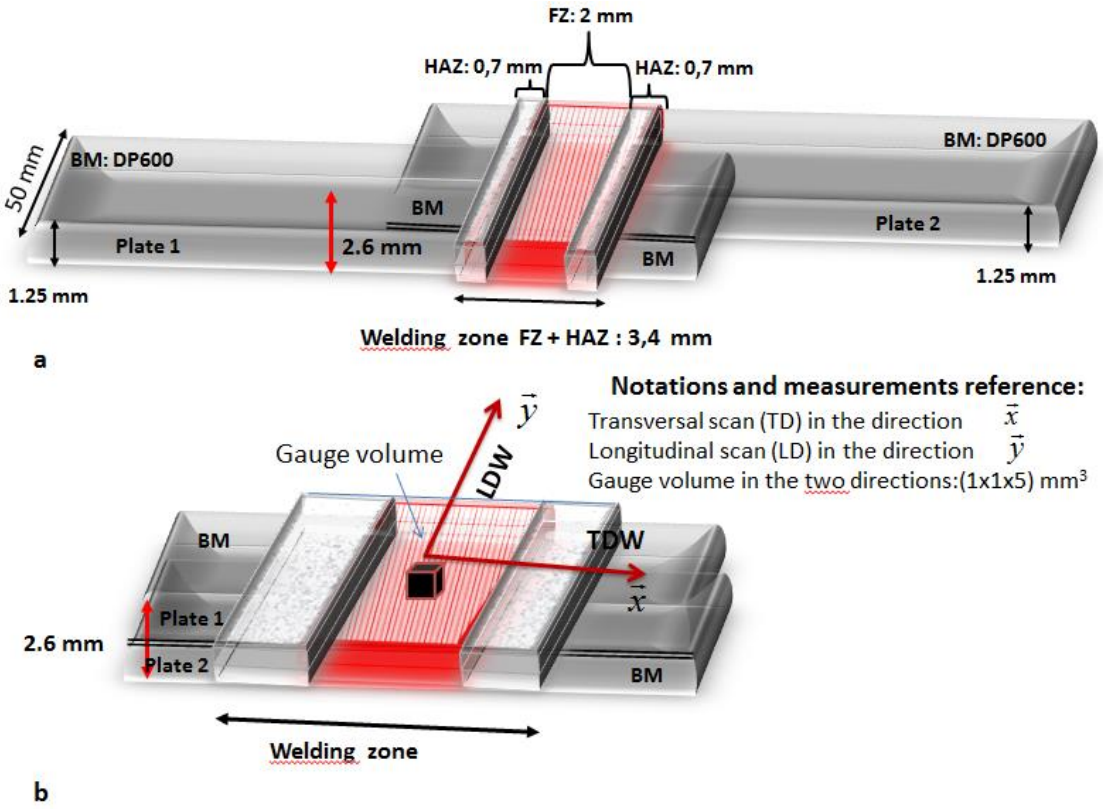

Fig.3: a) Welded plates of DP 600 steel, b) Experimental sketch for neutron diffraction,

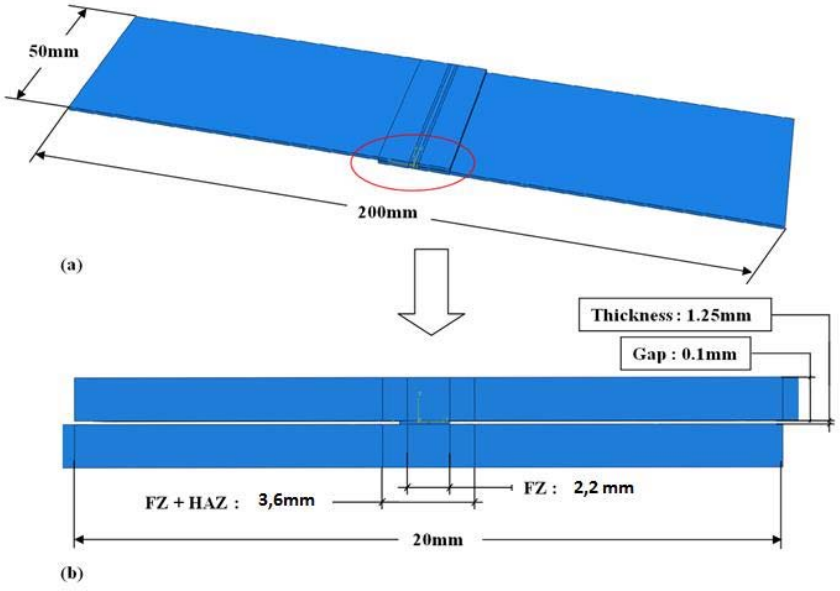

Fig.4: Model of sheet joint

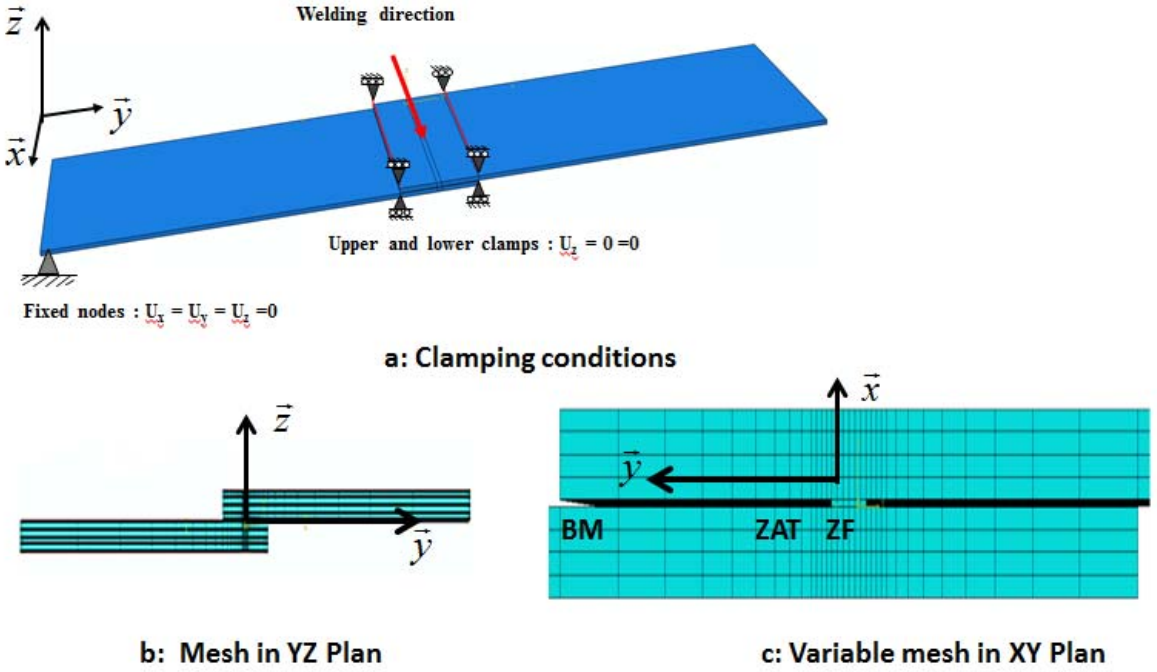

Fig.5: a) Clamping conditions, b and c) Mesh of the sheet metal model in YZ and XY plans

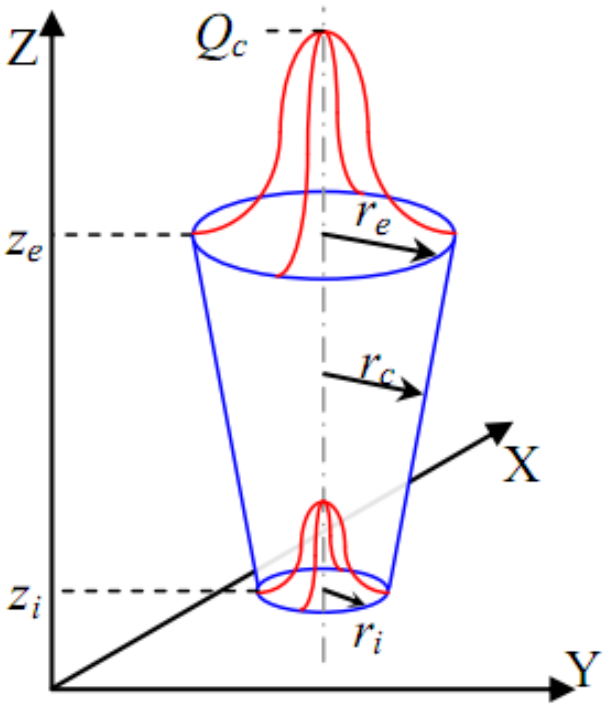

Fig.6: Conical heat source

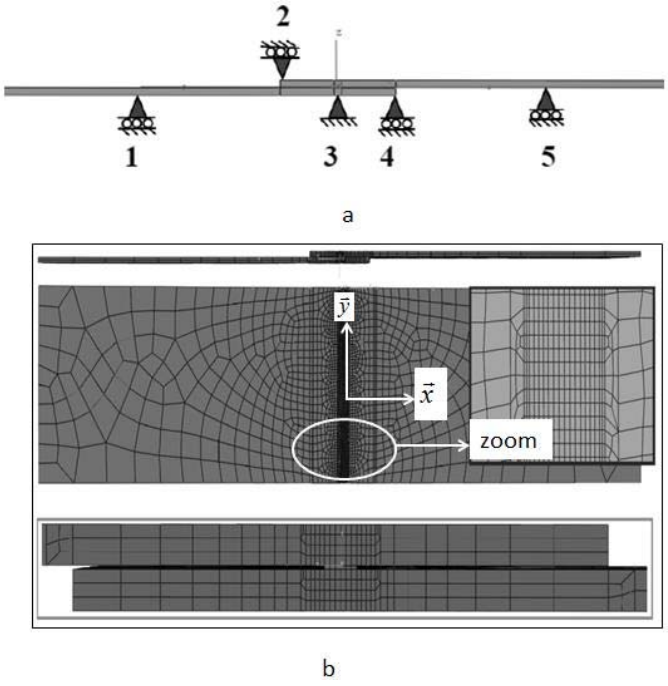

Fig. 7 a) Mechanical boundary conditions, b) Meshing elements

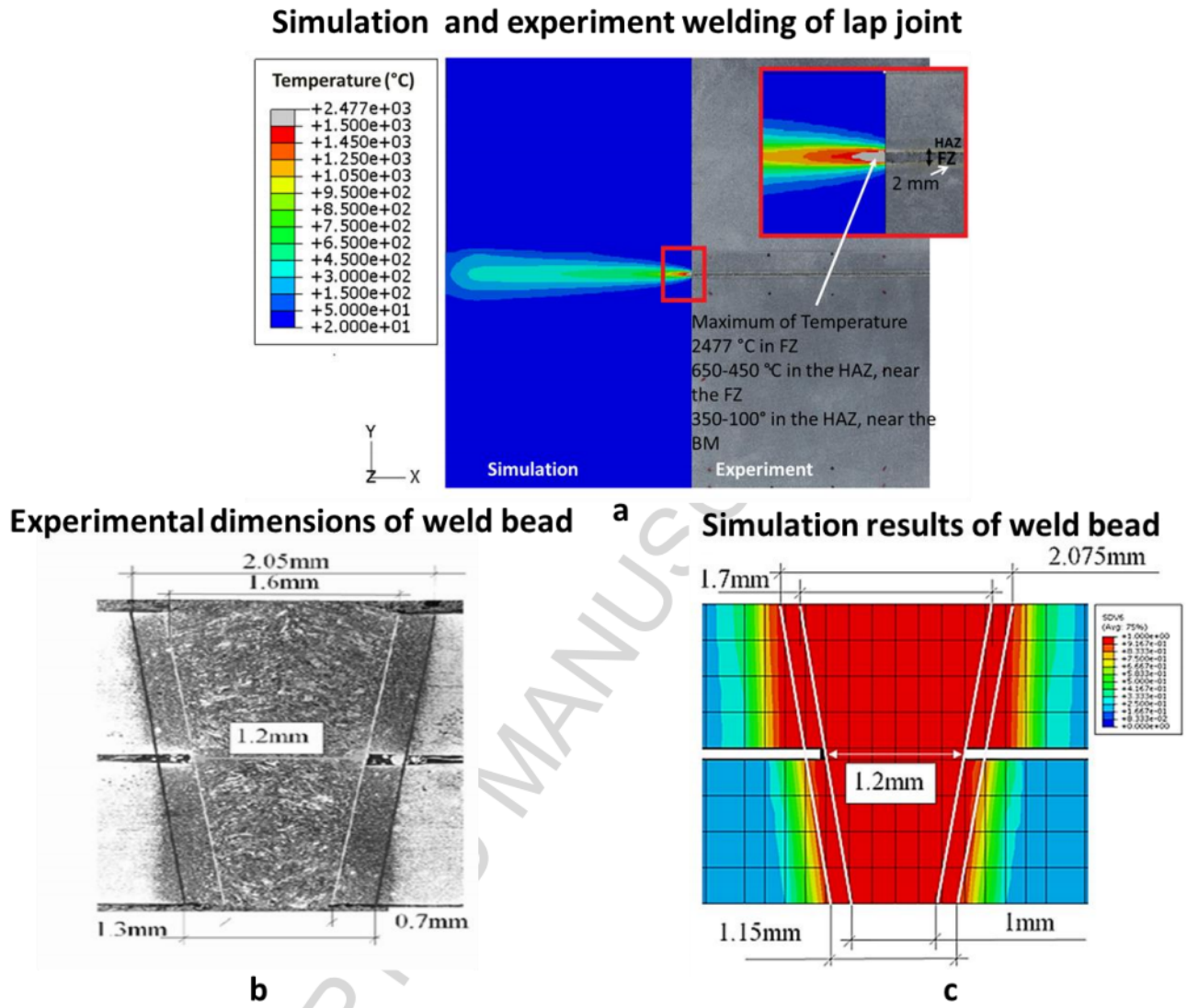

Fig.8 Cross section weld joint: comparison simulation and experiments

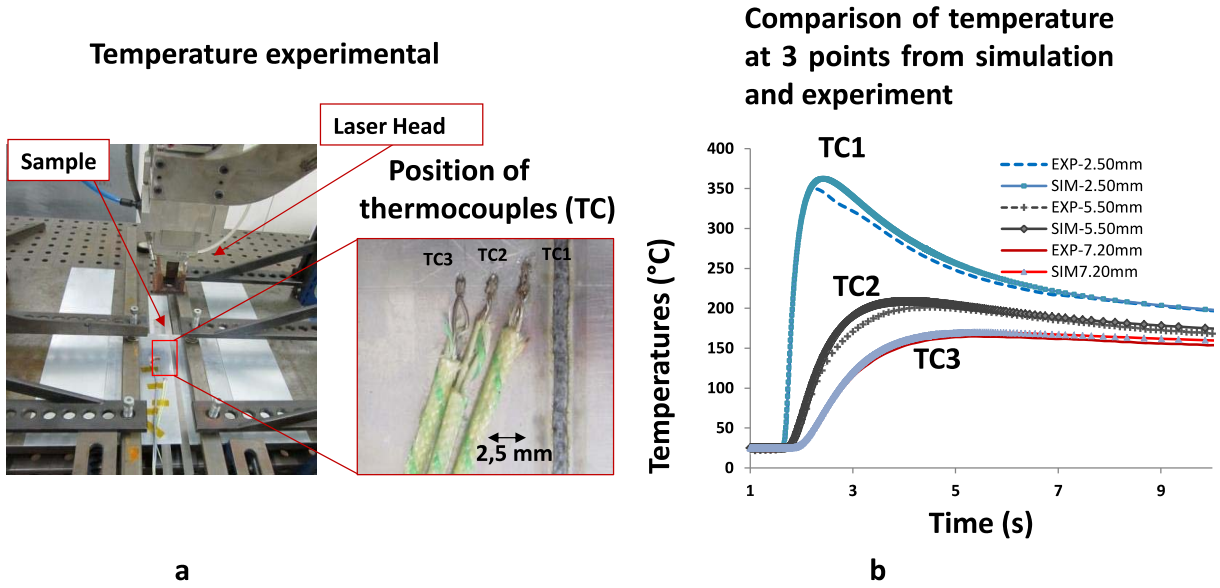

Fig.9 Temperature evolution: comparison experiment and simulation

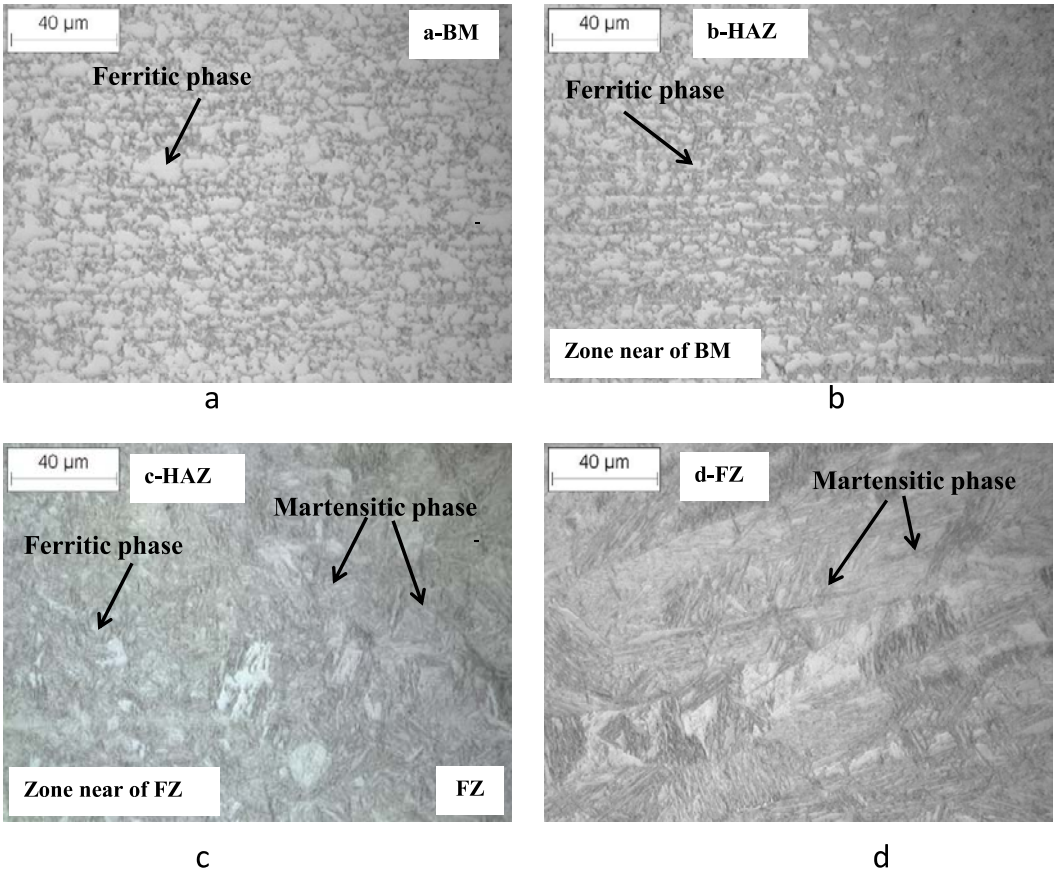

Fig.10: Micrographs from the different microstructures on top of the surface: a– Base Material; b and c- Heat Affected Zone and d- Fusion Zone

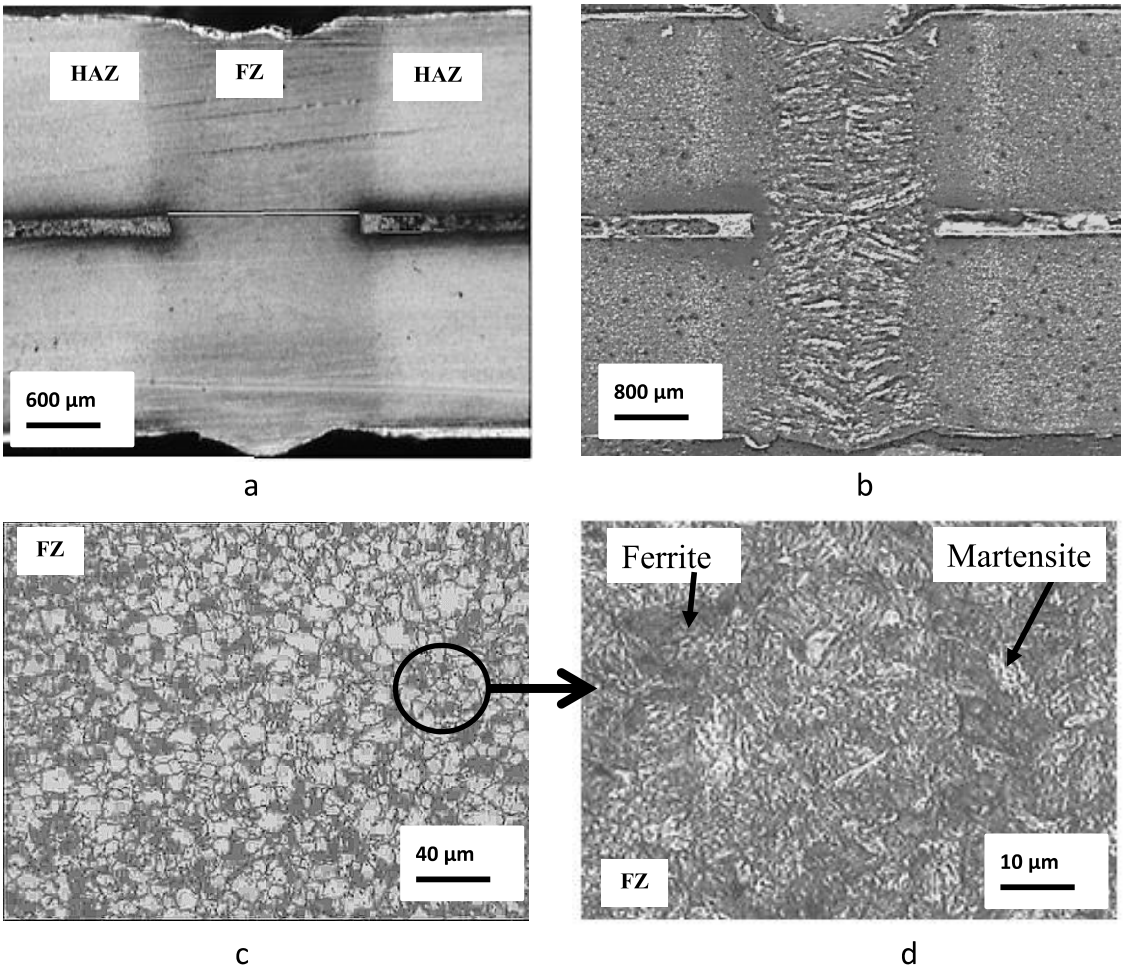

Fig.11: Micrographs from the different microstructures in the deep of the fusion zone for a full penetration: a– global zone of the weld bead; b- macroscopic zone, c- Microscopic zone in the deep and d- zoom of the zone fusion.

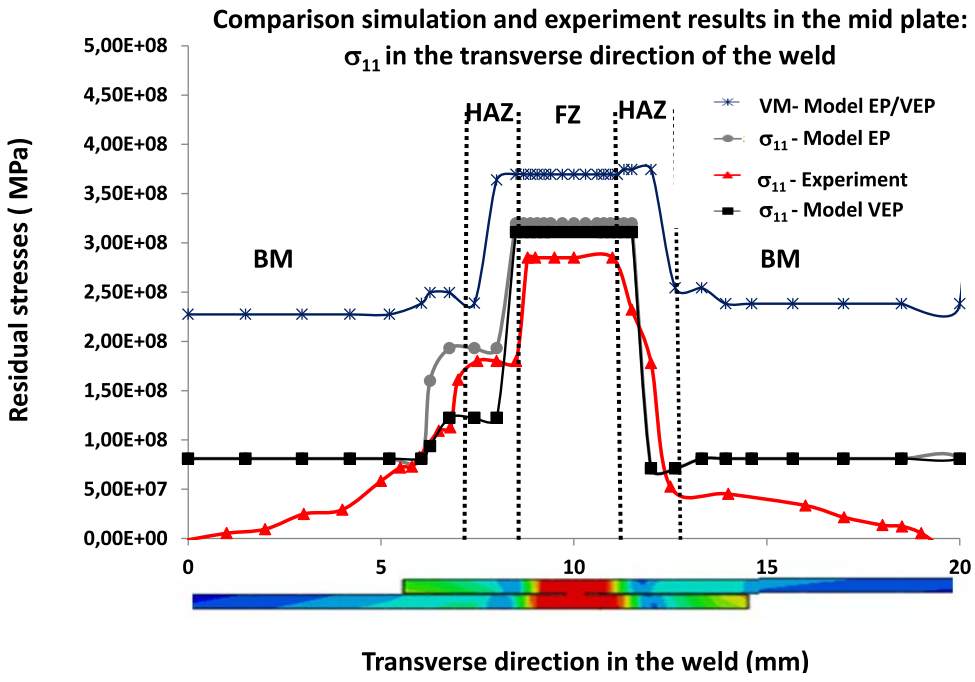

Fig.12: Transversal residual stresses on the mid steel plate with E=220MPa and Poisson's ratio = 0.33

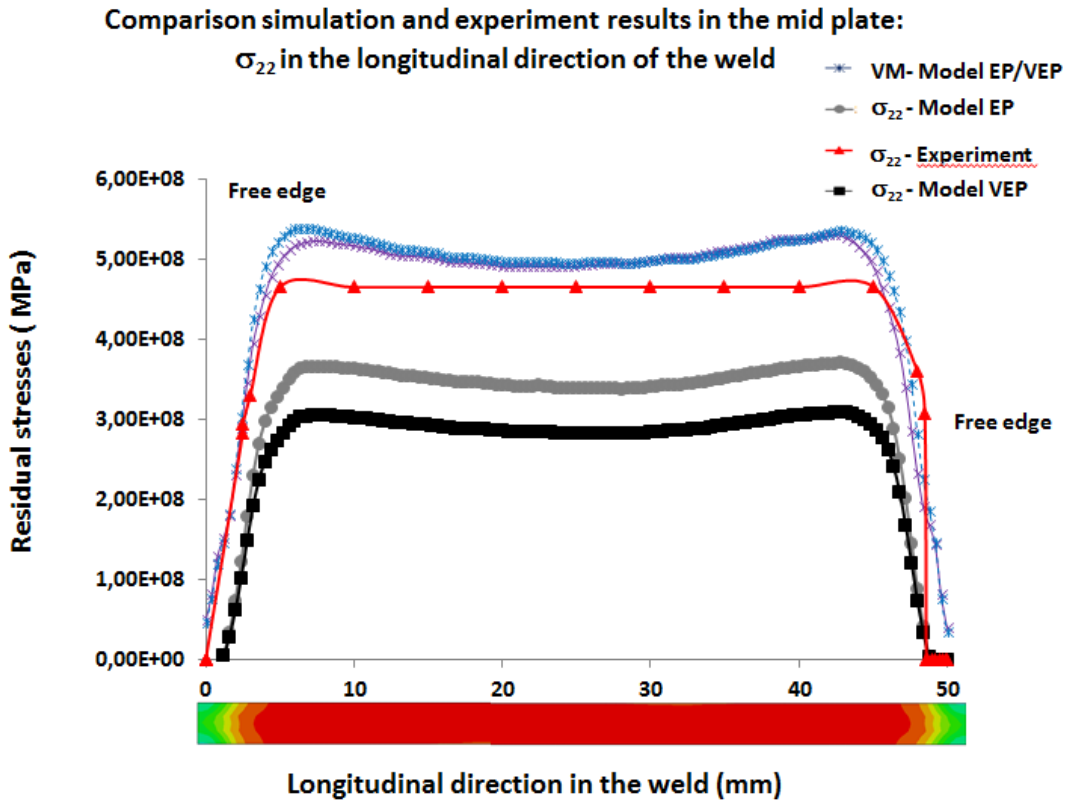

Fig.13: Longitudinal residual stresses on the mid steel plate considering E=220 MPa and Poisson's ratio = 0.33

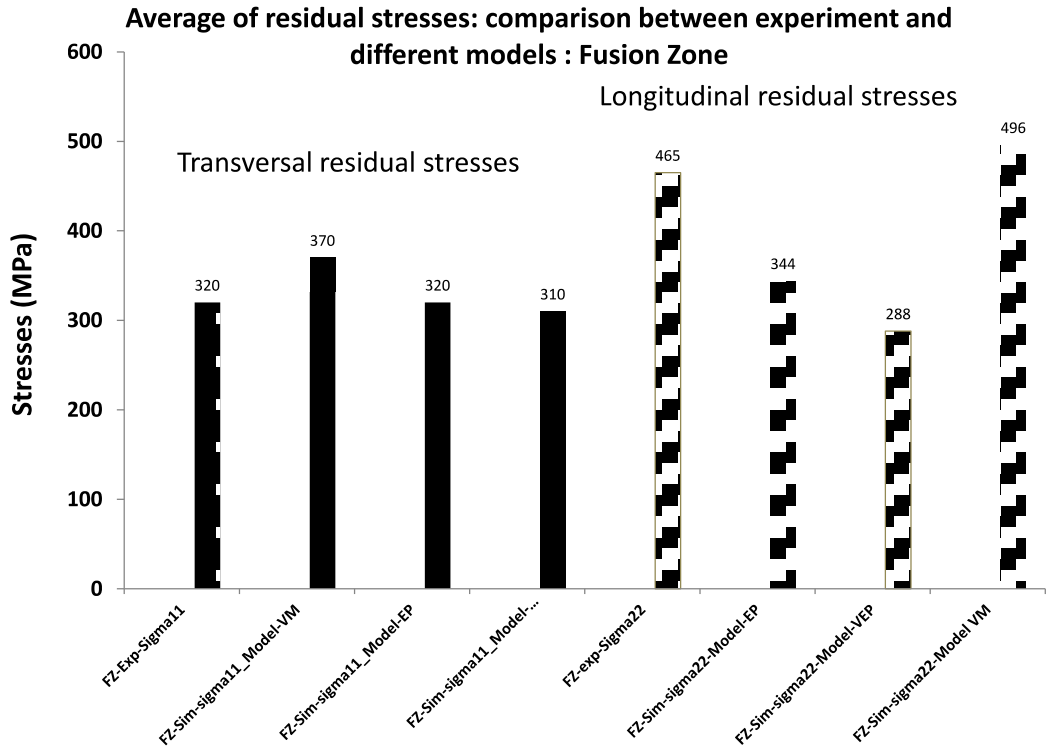

Fig.14: Average of residual stresses in the ferrite along the transverse line in the mid plates in the FZ

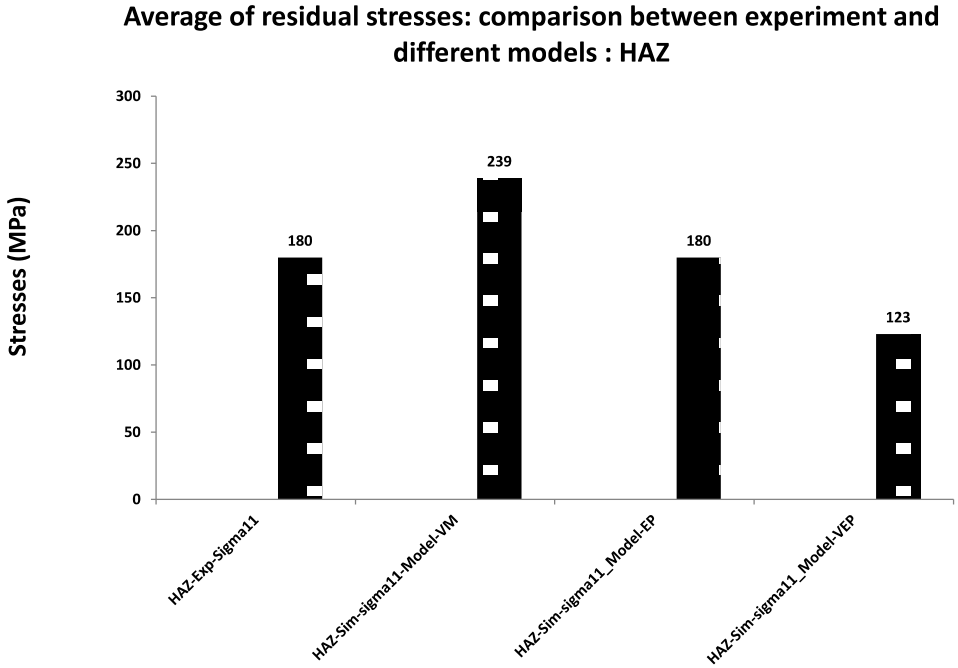

Fig.15: Average of residual stresses in the ferrite in the HAZ in the mid plates

Tables

Table 1
Parameter of thermal mesh size (mm)

Model	Zone1			Zone 2	Zone 3[a]
	DX	DY	DZ	DY	BIASE
M4	0.25	0.2	0.3125	0.175	10:17

[a]10:17 means 17 elements with biases factor of 10 from the small and the bigger one.

Table 2
Mechanical properties of high strength steel

Material	Yield Stress (MPa)	Ultimate Tensile Strength (MPa)	Total Elongation (%)
DP600	350	600	24-30

Table 3
Thermal properties of DP600 for FE analyses

Thermal property of DP600			
Temperature (^{o}C)	**Specific Heat Capacity (J/kg.°C)**	**Temperature (^{o}C)**	**Thermal Conductivity (W/m.°C)**
0	520	0	34.6
200	550	25	34.8
400	600	200	35
600	750	254	35
740	1160	1100	21.4
800	690	1200	25.5
1100	520	1300	60
1200	610	1400	70
3000	620	3000	70

Table 4
Parameter of Heat Source Model

Symbol	Quantity	Values
r_e	radius superior of cone	0.8 m^{-6}
r_i	radius inferior of cone	0.35 m^{-6}
r_c	distribution radius	m^{-6}
z_e	position in Z axis of r_e	2.6 m^{-6}
z_i	position in Z axis of r_i	0 m^{-6}
P	laser power used	3.5 kW
η	Efficiency	42%
V	welding speed used	3.4 m/min

Table 5
Thermo metallurgical expansion coefficient of DP600

Thermo metallurgical expansion coefficient of DP600	
γ-base (Austenite)	$2.13\ 10^{-5}$
α-base (FM, M)	$1.68\ 10^{-5}$
$\Delta\varepsilon_{\alpha\gamma}^{25°C}$	0.01375

Table 6
Mesh size of FZ and HAZ

	FZ-HAZ	Ratio in BM
DX	1 mm	125:62:31:25:10
DY	1 mm	5:15
DZ	5 mm	4:3:2

Graphical abstract

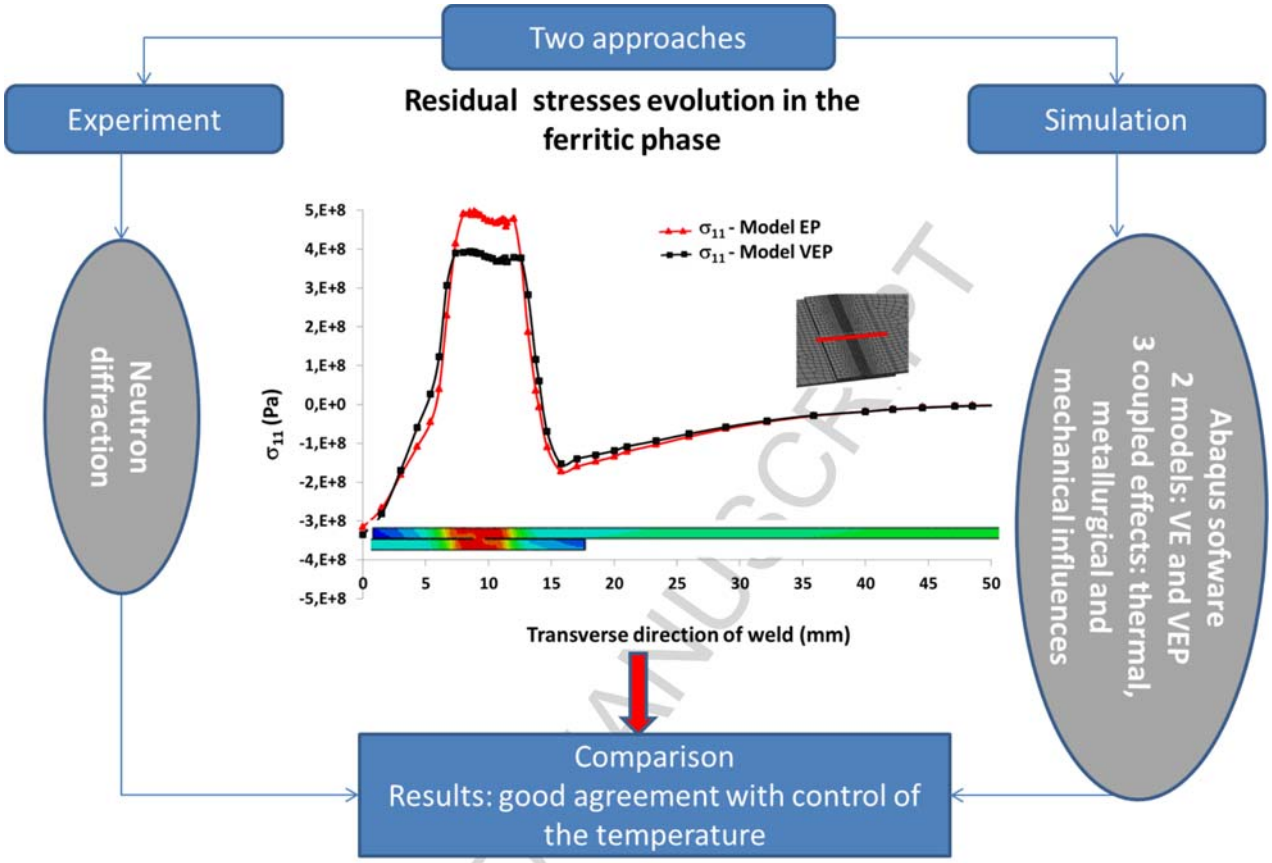

Highlight

- A Finite Element Method was developed to simulate welding residual stresses in dual phase steel.
- The residual stresses through the welded joint can be evaluated by FEM.
- The coupled effects with thermal, metallurgical and mechanical behaviors were uncovered.
- The validated FEM gives insights into the whole process of laser beam heat flux
- Experimental approach by neutron diffraction confirms the numerical approach.